Narrowband Oscillations in the Upper Equatorial Ocean. Part II: Properties of Shear Instabilities

W. D. SMYTH, J. N. MOUM, AND J. D. NASH

College of Oceanic and Atmospheric Sciences, Oregon State University, Corvallis, Oregon

(Manuscript received 17 February 2010, in final form 17 August 2010)

ABSTRACT

Narrowband oscillations observed in the upper equatorial Pacific are interpreted in terms of a random ensemble of shear instability events. Linear perturbation analysis is applied to hourly averaged profiles of velocity and density over a 54-day interval, yielding a total of 337 unstable modes. Composite profiles of mean states and eigenfunctions surrounding the critical levels suggest that the standard hyperbolic tangent model of Kelvin–Helmholtz (KH) instability is a reasonable approximation, but the symmetry of the composite perturbation is broken by the stratification and vorticity gradient of the underlying equatorial undercurrent. Unstable modes are found to occupy a range of frequencies with a peak near 1.4 mHz, consistent with the frequency content of the observed oscillations.

A probabilistic theory of random instabilities predicts this peak frequency closely. An order of magnitude estimate suggests that the peak frequency is of order N, in accord with the observations. This results not from gravity wave physics but from the balance of shear and stratification that governs shear instability in geophysical flows. More generally, it is concluded that oscillatory signals with frequency bounded by N can result from a process that has nothing to do with gravity waves.

1. Introduction

The upper equatorial oceans exhibit strong shear and stratification as well as evidence of small-scale instability (e.g., Moum et al. 1992; Hebert et al. 1992), but their mean profiles generally exhibit $\mathrm{Ri} > 1/4$, indicating stability. (Here, Ri is the gradient Richardson number, to be defined in detail below. Values $> 1/4$ indicate suppression of shear instability by stratification.) It has been suggested that random events such as internal gravity wave interactions perturb the flow locally so as to reduce Ri below $1/4$, setting the stage for shear instability (e.g., Moum et al. 1992; Peters et al. 1994). When resolution is fine enough to reveal regions where $\mathrm{Ri} < 1/4$, conditions amenable to instability can often be identified (e.g., Sun et al. 1998). Shear instabilities have also been seen in numerical simulations of the upper equatorial ocean (Skyllingstad and Denbo 1994; Wang et al. 1998; Wang and Müller 2002; Pham and Sarkar 2010).

In a companion paper, Moum et al. (2011, hereafter Part I) report on observations of a persistent narrowband signal in the upper equatorial Pacific from highly resolved measurements of temperature fluctuations on a mooring. This signal was characterized by a spectral peak (at frequency $f_{\mathrm{NB}} \simeq 0.001 - 0.002$ Hz) that was close to $N/2\pi$. The amplitude of the spectral peak varied diurnally (more energetic at night) and was correlated with enhanced turbulence. The signal was vertically coherent over the range of measurements (29–59 m) with an abrupt vertical phase change ($\pi/2$ over 20 m).

To examine aspects common to the observed signal and to shear instabilities, several properties of an ensemble of unstable modes determined from linear stability analysis (LSA) of observed currents and stratification were used for comparison. Most importantly, it was found that computed shear instabilities showed a preferred frequency very close to that of the observed oscillations (Fig. 1). The computed wavelengths were consistent with Kelvin–Helmholtz (KH) instabilities on a stratified shear layer and with previous observations that define their spatial structure (Moum et al. 1992). A particularly intriguing feature of both observed and computed frequency distributions is that the peak frequency lies close to the local buoyancy frequency N. This property calls to

Corresponding author address: W. D. Smyth, College of Oceanic and Atmospheric Sciences, Oregon State University, 104 Ocean Admin. Bldg., Corvallis, OR 97331.
E-mail: smyth@coas.oregonstate.edu

DOI: 10.1175/2010JPO4451.1

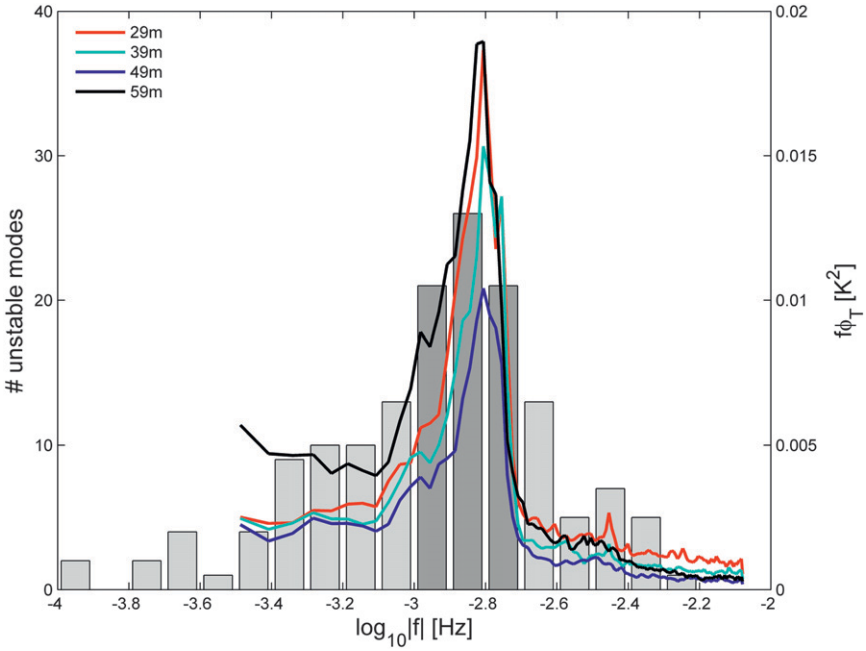

FIG. 1. Histogram of absolute cyclic frequency for 155 unstable modes computed numerically from hourly averaged profiles of velocity and density (see section 3 and appendix A for details). Dark bars highlight the peak frequency range used in later analyses. Curves show variance-preserving spectra of four independent χpod temperature time series, averaged over the entire time period and normalized to make the maximum value 40. Sensor depths are as shown in the legend.

mind internal gravity waves (IGWs), whose intrinsic frequency is bounded by N. In contrast, the frequency of a KH billow is essentially independent of N, and it seems suspicious that the two should happen to be of such similar magnitude.

Our goal in the present paper is twofold. First, we provide a thorough description of the unstable modes and the assumptions and methods by which they are derived. In the process, we show how linear eigenfunctions can be used in making quantitative estimates of vertical velocities, fluxes, and dissipation rates. Second, we explore a probabilistic model that accounts for the near-N frequencies of the observed oscillations. We imagine that the upper equatorial Pacific exists in a state of near-neutral equilibrium, with shear somewhat less than that required to produce instability. At random times and places, that equilibrium is upset locally (perhaps by the constructive interference of gravity wave packets), leading to a local increase in shear and hence to the potential for instability (Miles 1961; Howard 1961). Each instability grows and then mixes out, returning the mean flow to a stable state. We hypothesize that the observed oscillations represent the net effect of these sporadic mixing events.

To test this hypothesis, we treat the hourly averaged profiles of velocity and density as stationary states and assess their stability against normal mode perturbations. The profiles are described briefly in section 2 (and thoroughly in Part I). We scan the 1296 h of the observation period and, for each hour, look for sites of potential instability (section 3). The resulting unstable modes are compared with the observed oscillations. In section 4, statistics of various model parameters are examined, extending the analyses of Part I. In section 4b, a composite of the mean flow surrounding unstable modes with frequencies near the peak is shown to look a lot like a textbook shear layer, justifying preliminary identification of the instabilities as KH, but also revealing some intriguing similarities with the ''near jet'' model of Pham and Sarkar (2010).

The connection between mode frequency and N is pursued in two steps. First, we derive a simple probability distribution function for frequency based on uniform distributions of wavelength and phase velocity (section 5a). This yields a peak frequency very close to that found in both the linear stability analyses and in the observations. We then show, in section 5b, that the peak frequency is of order N. Conclusions are summarized in section 6.

2. Observational context

The background states for our stability analyses were taken from the Tropical Atmosphere Ocean (TAO) array between 19 December 2006 and 10 February 2007, inclusive (Fig. 2); details of the measurements and data

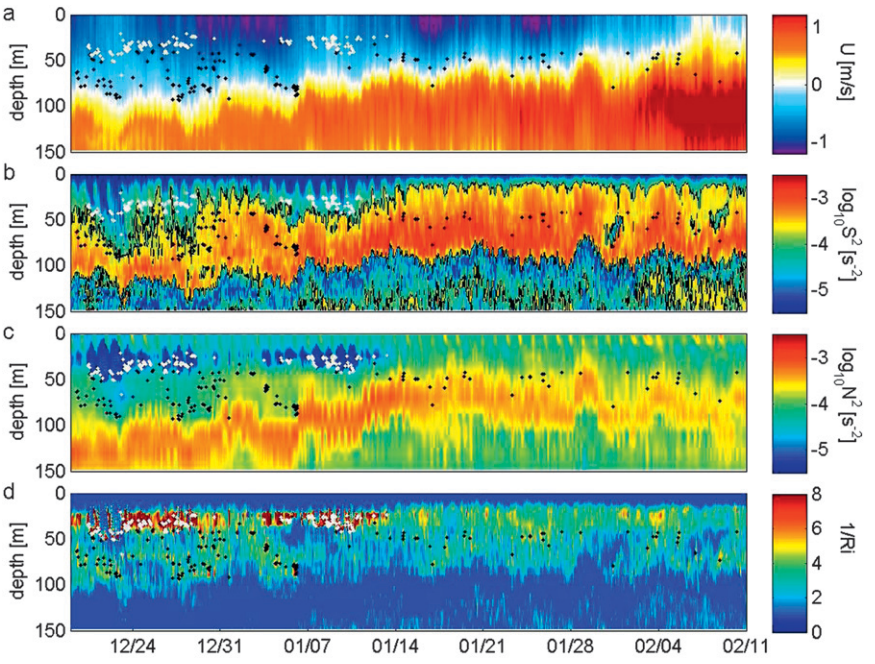

FIG. 2. Flow characteristics in the upper 150 m: (a) zonal velocity, (b) squared shear, (c) squared buoyancy frequency, and (d) inverse Richardson number. White bullets indicate "shallow" modes; black bullets indicate the "deep" modes that are the focus of the discussion to follow. The black contour in (b) encloses regions with $S^2 > 1.31 \times 10^{-4}$ s^{-2}, used to identify the deep, rapidly growing modes.

processing are given in section 3a. Early in the analysis period, the west-flowing South Equatorial Current (SEC) was unusually deep and strong (blue in Fig. 2a). Through January, the SEC relaxed and shallowed, and by February a strong Equatorial Undercurrent (EUC, shown in red) was evident near 100-m depth. Meridional velocities were weak during this interval and are not shown. Shear and stratification were both strongest on the upper flank of the EUC (Figs. 2b and 2c). For later reference, note that in late December when the SEC was deep, unusually weak stratification (blue) extended to nearly 100-m depth. The inverse Richardson number frequently exceeded the critical value 4, indicating the potential for instability (Fig. 2d).

The TAO moorings were supplemented by moored χpods over several months in 2006–07, yielding extended, high-resolution time series of temperature at 0°, 140°W and at four depths: 29, 39, 49, and 59 m. From these measurements arises a new depiction of the full frequency spectrum of temperature fluctuations (Fig. 1) through to the frequencies associated with turbulence, from which the turbulent dissipation rates are estimated. In Part I, we found that each series showed a persistent spectral peak near the cyclic frequency 1.4 mHz. Oscillations appeared in groups of ~10, and were associated with elevated turbulent dissipation rates that could have accounted for their demise. These oscillations showed several "textbook" features of KH instability.

1) The waves were vertically coherent at the peak frequency and showed a phase difference of about 90° across the shear layer.
2) Taking the layer over which the phase changed as the inner half of the shear layer, we estimate that the wavelength would be 7 times greater, for example, $7 \times 20 = 140$ m. This is in the range of previous observations (Moum et al. 1992).
3) Combining this wavelength and the measured frequency gives a phase velocity that is within the range of the background current profile, as predicted for shear instability by the Howard (1961) semicircle theorem.

Absence of any of these three properties would have disproved the hypothesis that the oscillations are KH events, and their confirmation encourages us to explore the hypothesis further.

3. Methodology for linear stability analysis of measured profiles

a. Processing of TAO data for stability analysis

Hourly profiles of velocity–shear and density–stratification were derived from TAO mooring data at 0°, 140°W. Because

LSA is sensitive to $\partial u/\partial z$ and $\partial \rho/\partial z$, data were carefully processed to prevent artifacts in vertical gradients when gridded onto the 1-m LSA grid. First, density was computed from collocated T and S at 1-, 5-, 10-, 20-, 40-, 60-, 80-, and 120-m depths. These were augmented by T-only sensors at 28, 100, and 300 m; to compute density, S was linearly interpolated at 28- and 100-m depths, and assumed constant below 120 m. Then, $\partial \rho/\partial z$ was computed using first differences at midpoints between sensors, and $\partial \rho/\partial z$ linearly interpolated onto the fine-resolution grid. Finally, density was computed by integrating $\partial \rho/\partial z$. Velocity profiles were computed from a secondary subsurface mooring (typically located 1000 m away) with an upward-looking 150-kHz acoustic Doppler current profiler (ADCP), mounted nominally at 290 m, recording data in 8-m bins, but linearly interpolated onto a 5-m grid. Above 40-m depth (where ADCP data are contaminated by sidelobe reflections), discrete u and v measurements from Argonaut point sensors located on the primary mooring at 10, 25, and 45 m were used. As with density, shear was computed based on first differences at midsensor locations (i.e., at 12.5 and 35 m) and, then, linearly interpolated onto a 1-m grid; for simplicity and stability, $\partial \rho/\partial z = 0$ at $z = 0$ was assumed. Finally, velocity was computed by integrating shear.

b. Linear stability analysis

The linear perturbation theory for a viscous, diffusive, stratified shear flow is reviewed in appendix A, along with numerical techniques for the solutions of the resulting equations. Here, we describe aspects of the methodology specific to the present application.

The hourly averaged profiles of zonal velocity and buoyancy (section 3a) were tested for stability against normal mode perturbations of the form

$$\phi'(x, y, z, t) = \hat{\phi}(z) \exp[\sigma t + i(kx + ly)]. \qquad (1)$$

Here, ϕ' represents a two-dimensional perturbation of any flow property; $\hat{\phi}$ is a complex, z-dependent eigenfunction; σ is a complex growth rate; and k, l is a real wavenumber with zonal and meridional components. Only the real part of ϕ' is physically relevant. The wavenumber is related to the wavelength λ by $\lambda = 2\pi/\tilde{k}$, where $\tilde{k}$ is the wavenumber magnitude $\sqrt{k^2 + l^2}$. Departure of the wavevector from the positive zonal direction is measured by the obliquity angle $\theta = \tan^{-1}(l/k)$. The negative imaginary part of the growth rate, $-\sigma_i$, is a radian frequency, sometimes denoted ω. The phase velocity is given by $c = \omega/\tilde{k}$, and the depth at which the phase speed matches the background flow in the direction of (k, l) is called the critical level z_c.

The wavenumber plane was scanned for local maxima of the growth rate. Any case for which the minimum Richardson number ($\mathrm{Ri} = N^2/S^2$, where N and S are the buoyancy frequency and shear magnitude of the mean state, respectively) was greater than 1/4 was skipped, as it failed to satisfy the Miles (1961) necessary condition for instability. Any growth rate maximum was identified as a growing instability and retained for analysis subject to the following additional criteria.

1) Velocity measurements do not resolve vertical scales less than 16 m. A shear layer with thickness one-half of this value is expected to produce an instability with wavelength approximately $7\ \mathrm{m} \times 8\ \mathrm{m} = 56$ m (Hazel 1972). Accordingly, only modes with wavelength greater than 56 m are retained.
2) Because it treats the mean flow as stationary, the stability analysis is only valid when the resulting instability grows on a time scale faster than any fluctuation in the mean flow. The fastest fluctuations allowed in our data are those occurring on time scales similar to the averaging interval, 1 h. Accordingly, we reject any mode with growth rate σ_r less than $1\ \mathrm{h}^{-1}$.
3) Nocturnal surface mixed layers are distinguished from the underlying fluid by very weak shear and stratification. Unstable modes with critical layers in this regime have very different physical characteristics and are thus identified as a separate mechanism (the ''shallow'' modes shown as white dots in Fig. 2). These are eliminated by imposing the criterion $S_c^2 > S_{c0}^2$, where $S_{c0}^2 = 1.31 \times 10^{-4}\ \mathrm{s}^{-2}$ (contour in Fig. 2b), where S_c^2 is the squared shear at the critical level. The critical-level Richardson number, $\mathrm{Ri}_c = N_c^2/S_c^2$, is $<1/4$ for all modes, but can be $\ll 1/4$ for the shallow modes (Fig. 3).

For computational efficiency, the (k, l) plane was scanned using two grids. The first had values of k and l spaced logarithmically, with successive values differing by a factor 1.27. Values of k corresponded to zonal wavelengths $2\pi/k$ ranging from 56 to 400 m. (Preliminary trials showed no unstable modes at wavelengths greater than this.) Values of l were the same as those of k, plus their negatives, plus zero. Velocity and density profiles were interpolated to a vertical spacing of 1.5 m using cubic splines. The computational domain extended from the surface to 200-m depth. This grid was scanned, keeping the largest σ_r at each (k, l), and wherever a local maximum in σ_r exceeding $1\ \mathrm{h}^{-1}$ was found, a second scan was performed. For the second scan, only a small region of the wavenumber plane surrounding the maximum was covered. This enabled us to halve the grid spacing in the k, l plane; extend the domain to 250-m depth; and reduce the vertical grid spacing to 1 m. Sensitivity tests established that this vertical resolution and this domain depth are

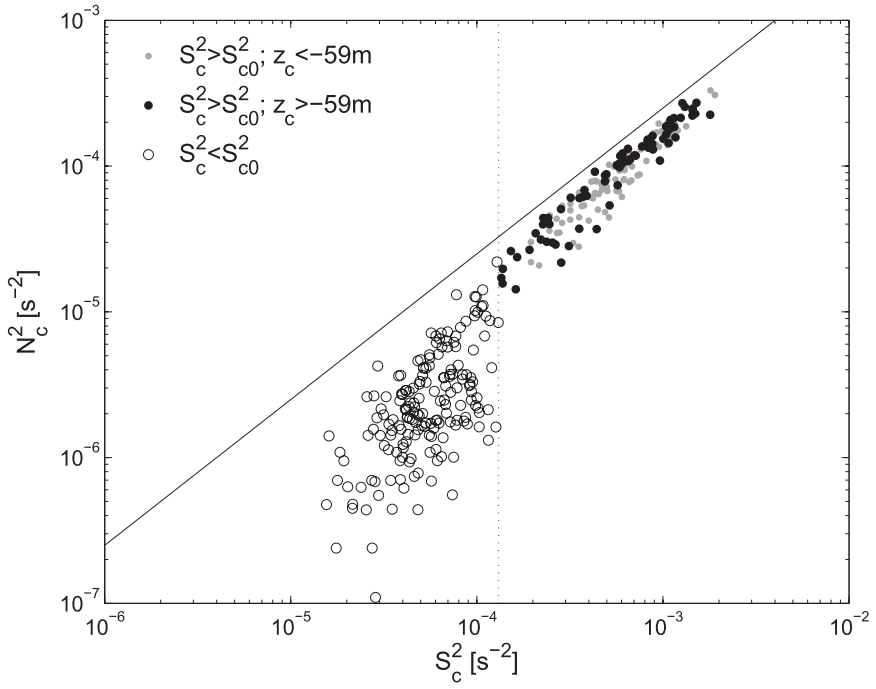

FIG. 3. Squared buoyancy frequency vs squared shear at the critical level for 334 unstable modes. Bullets and open circles indicate deep and shallow modes, respectively. The vertical dotted line at $S_c^2 = S_{c0}^2$ delineates the mode categories. The slanted line indicates $N_c^2/S_c^2 = 1/4$. Gray bullets represent modes with critical levels deeper than the deepest χpod.

sufficient for the resulting eigenmodes to converge. If the local maximum still satisfied the growth rate criterion, a biquadratic fit was performed over the nearest 13 grid points and used to make a further estimate of the location of the growth rate maximum. If that estimate yielded a larger growth rate, it was retained; if not, it was discarded in favor of the maximum gridded value.

The algorithm identified 375 modes that satisfied criterion 1. Of these, 47 were rejected on the basis of criterion 2, leaving 334. Criterion 3 allowed us to identify 182 of these as shallow modes (Fig. 3, white dots in Fig. 2). Removing these left 152 modes (black dots in Fig. 2) for further analysis. The majority of the retained modes occurred in December and early January when the SEC was deep and weak stratification, ordinarily characteristic of the near-surface layer, extended to 100-m depth. As expected, modes generally coincide with regimes of elevated shear (Fig. 2b) and inverse Richardson number (Fig. 2d).

4. Characteristics of the unstable modes

a. Eigenvalue statistics

The scalar properties of our ensemble of instability events are summarized in Figs. 1, 4, and 5. The growth rates (Fig. 4a) covered the same range throughout the analysis period. As noted previously, a large fraction of the instabilities appeared in December and early January. Although modes were found as deep as 70–90 m (Fig. 2), their phase velocities (Fig. 4b) were dominantly negative since the west-flowing SEC was unusually deep during that time. In mid- to late January and early February, instabilities were sparser and tended to concentrate at shallower depths, consistent with the shoaling of the EUC (Fig. 2). By February, phase velocities were generally positive, consistent with critical levels located in the east-flowing EUC.

Many of the modes found early in the analysis period were located below $z = -59$ m, the depth of the deepest χpod. As modes flux buoyancy primarily downward (e.g., Fig. 7 below), these deep modes may be difficult to detect with the χpods. The deep modes are shown as gray bullets in Fig. 4. When these are ignored, the distribution over time is much more consistent with the time dependence of the observed oscillations. The observed trend to lower frequencies over time (Part I, Figs. 3c–f and 8a) is also reflected in these modes (Fig. 4c).

Histograms derived from the entire ensemble shown in Fig. 4 provide a more comprehensive view of the mode properties. The growth rates (Fig. 5a) range from 1 to 11

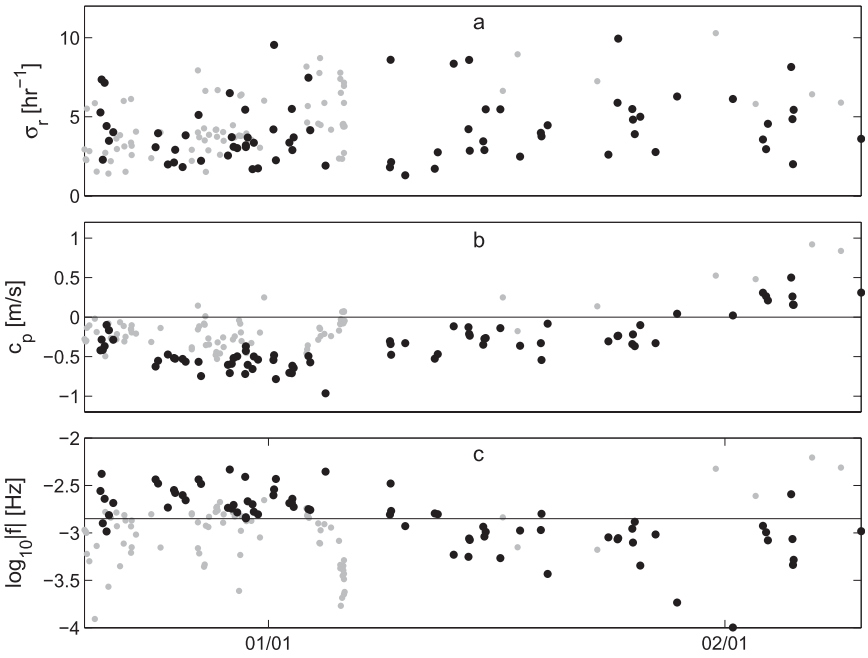

FIG. 4. (a) Growth rates, (b) phase velocities, and (c) absolute cyclic frequencies of computed unstable modes, displayed as a function of time. Black bullets indicate modes with critical levels within the range of the χpods (above 59-m depth). Gray bullets represent modes with critical levels deeper than 59 m. The horizontal line in (c) indicates $\log_{10}|f| = -2.85$, the peak frequency from Fig. 1.

e-foldings per hour with a peak at 4 h^{-1}.[1] Because the background flows were primarily zonal, the obliquity angle θ was most commonly near zero (Fig. 5b). The cyclic frequencies ($f = \sigma_i/2\pi$) are generally negative (Fig. 5c).

Phase velocities (Fig. 5d) cover most of the range of the zonal currents, from -1 m s^{-1} in the SEC to $+1$ m s^{-1} in the EUC. Negative values are considerably more common because of the coincidence of weak stratification and a deep, strong SEC early in our analysis period. Critical-level depths (Fig. 5e) are restricted to values deeper than 37.5 m, and extend nearly to the depth of the EUC core. Although unstable modes might in principle have wavelengths up to 7 times the depth of the EUC core, or 700 m, most computed modes had λ between 100 and 350 m. Modes with horizontal wavelengths less than 56 m were rejected due to the limited vertical resolution of the measurements (section 3b, criterion 1). The computed range of wavelengths is consistent with existing observations (e.g., Moum et al. 1992) and stability analyses (e.g., Sun et al. 1998; Smyth and Moum 2002).

We have hypothesized that this ensemble of instability events is responsible for the high-frequency oscillations observed in the χpod records (Part I). This hypothesis is conveniently tested via comparison of the logarithmic distribution of mode frequencies with the variance-preserving spectra of the observed temperature time series. The histogram in Fig. 1 is the variance-preserving, logarithmic form of the frequency distribution shown in Fig. 5c. The solid curves show the time-dependent spectrogram from Part I (Fig. 3) averaged over the 54-day period of the analyses. Frequencies below 3×10^{-4} Hz are not shown as the spectrum is dominated by tidal motions in that range. Although these are two different indicators of the frequency content, we expect dominant features such as the narrowband peak to be reproduced.

Both the histogram and all four curves show a peak at $|f| = 1.7 \times 10^{-3}$ Hz with slightly elevated values at lower frequencies. This correspondence between the ensemble of unstable modes and four independent records of temperature fluctuations provides compelling evidence in support of our hypothesis.

[1] A more complete histogram would descend monotonically from a peak at $\sigma_r = 0$, representing the theoretically infinite population of marginally unstable modes. Our search algorithm finds the fastest-growing mode first, then iterates to find additional modes. The iteration must stop after a finite time, and it therefore rejects a large number of marginal modes. This is also evident in Fig. 3, where the gap between the instability ensemble and the stability boundary shows the absence of marginal modes. Figure 1 suggests that our algorithm successfully identifies the modes that contribute most to the observed signal.

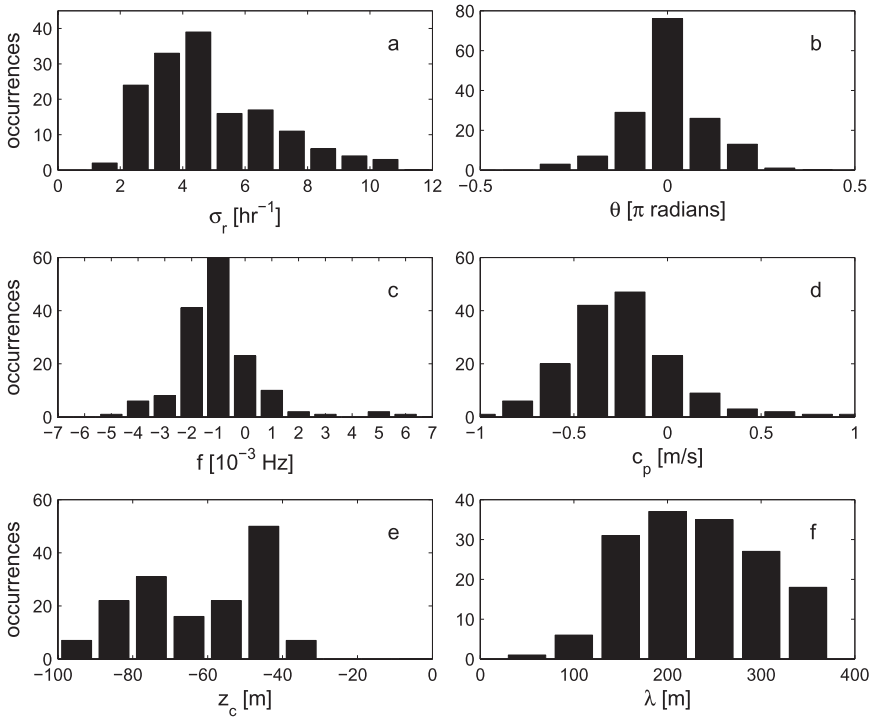

FIG. 5. Histograms of the (a) growth rate σ_r, (b) angle of obliquity, (c) cyclic frequency, (d) phase velocity c_p, (e) critical-level depth z_c, and (f) wavelength λ.

b. The composite mean flow

To assess the nature of the background states that produce the instabilities, we compiled profiles of velocity, shear, stratification, and Richardson number representative of the neighborhoods of 69 unstable modes near the peak frequency of the narrowband oscillations described in Part I. The modes were selected by the requirement that $\log_{10}|f|$ lie between -3.0 and -2.7 (dark bars in Fig. 1). A scaled depth was defined for each mode, measured from the critical level in units of the wavelength. Likewise, the velocity was measured relative to the phase velocity. The profiles were then sorted into 42 bins of the scaled depth ranging from -0.5 to 0.5. For each flow property, the median and upper and lower quartiles in each bin were computed. Results are shown in Fig. 6. Horizontal dotted lines indicate a layer of thickness $\frac{1}{7}$ the wavelength, the approximate ratio for KH instability on a shear layer.

The composite velocity profile (Fig. 6a) features a central shear layer bounded below by a jet corresponding to the EUC and above by a layer of much weaker shear. In the upper part of the central shear layer, the shear exhibits a distinct peak (Fig. 6b), which coincides closely with $z = z_c$. This is consistent with our scenario of a local increase in shear due to some random event.

The shear profile reveals a broader region of elevated shear below the main peak. This shear is stabilized by enhanced stratification associated with the EUC core (Fig. 6c). As a result, the inverse Richardson number (Fig. 6d) is below the critical value 4.

In contrast, the upper part of Fig. 6d shows Ri^{-1} close to and occasionally exceeding 4. We do not expect strong instability here as the high Ri^{-1} is caused by weak stratification, not strong shear. Only in a thin layer surrounding $z = z_c$ do we see strong shear combined with values of Ri^{-1} consistently greater than 4. The thickness of that layer corresponds quite well with the value $\lambda/7$ expected for a shear layer, as indicated by the horizontal dashed lines.

In summary, the composite background velocity profile close to the critical level is broadly consistent with the hyperbolic tangent model used previously to describe Kelvin–Helmholtz instability (e.g., Hazel 1972). The unstable shear layer is typically located near the upper edge of a thicker layer where the shear is stabilized by strong stratification. These secondary features are likely to have some effect on the stability characteristics. An alternate (and likely better) representation of this composite background flow state is the ''near jet'' case used recently in simulations of the EUC by Pham and Sarkar (2010).

c. The composite eigenmode: Quantitative predictions from linear theory

Figure 7 shows the composite vertical velocity eigenfunction, with the median composite current, shear, and

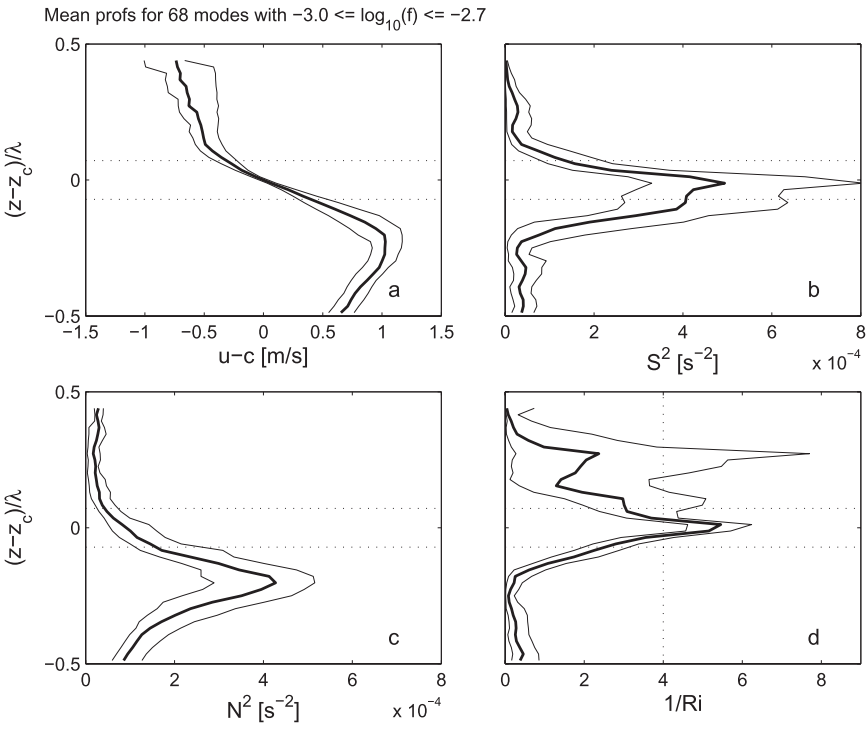

FIG. 6. Composite mean flow in the neighborhood of the critical level: (a) $u - c$, (b) S^2, (c) N^2, and (d) 1/Ri. Thick (thin) curves indicate the median (and upper and lower quartiles) of profiles around a sampling of 68 unstable modes with frequencies near the peak. Profiles are centered at the critical level, and the vertical coordinate is normalized by the wavelength. Horizontal dotted lines indicate a layer of thickness $1/7$ the wavelength.

stratification profiles for reference. Near the critical level, the vertical velocity is reduced and the eigenfunction undergoes a rapid phase shift. This pattern of behavior coincides with a thin layer in which $S^2 > 4N^2$ (or Ri $< 1/4$; cf. Figs. 7b and 6d) and is characteristic of shear instability. Below the critical level, large vertical velocities are seen in combination with a gradual tilt in phase (Figs. 7c and 7d), indicating wavelike behavior in the vertical (we return to this topic below).

The perturbation kinetic energy flux (Fig. 8b) diverges from the critical level, with a weak upward flux and a much stronger downward flux. Energy propagation is supported by both the stratification and the vorticity gradient in the underlying jet. To see this, consider the corresponding terms in the Taylor–Goldstein equation (e.g., Miles 1961):

$$\hat{w}_{zz} + \mu^2 \hat{w} = 0; \quad \mu^2 = \frac{N^2}{(U-c)^2} - \frac{U_{zz}}{(U-c)} - \tilde{k}^2. \quad (2)$$

The equivalent theory, with viscosity and diffusion included, is described in appendix A. When $|c_i| \ll |U - c_r|$, the condition $\mu^2 > 0$ indicates the potential for vertical wave propagation. The first term, representing gravity waves, is positive. The second term represents shear waves. These may be viewed as the small-scale analog of Rossby waves, as their restoring force results from the vorticity gradient U_{zz}. Below the critical level there is a local maximum in U at which $U - c > 0$, so this term is positive also. Quantitatively (Fig. 8c), wave propagation extends below the critical level to $z - z_c = -0.27\lambda$. Below this level, waves are evanescent. At $z - z_c = -0.14\lambda$, the nature of the wave switches: above that level it is mainly a gravity wave; below it is mainly supported by shear. In a thin region above the critical level (extending to $z - z_c = 0.15\lambda$) wave propagation is possible, but critical-level interactions for these modes are such that little propagation occurs.

The momentum and buoyancy fluxes, computed as in appendix A, are focused mainly near the critical level (Figs. 9b and 9c). The momentum flux is positive, indicating a downward flux of westward momentum from the SEC. The buoyancy flux is downward. Both fluxes are elevated in the region below the critical level corresponding to the EUC, again indicating downward energy propagation.

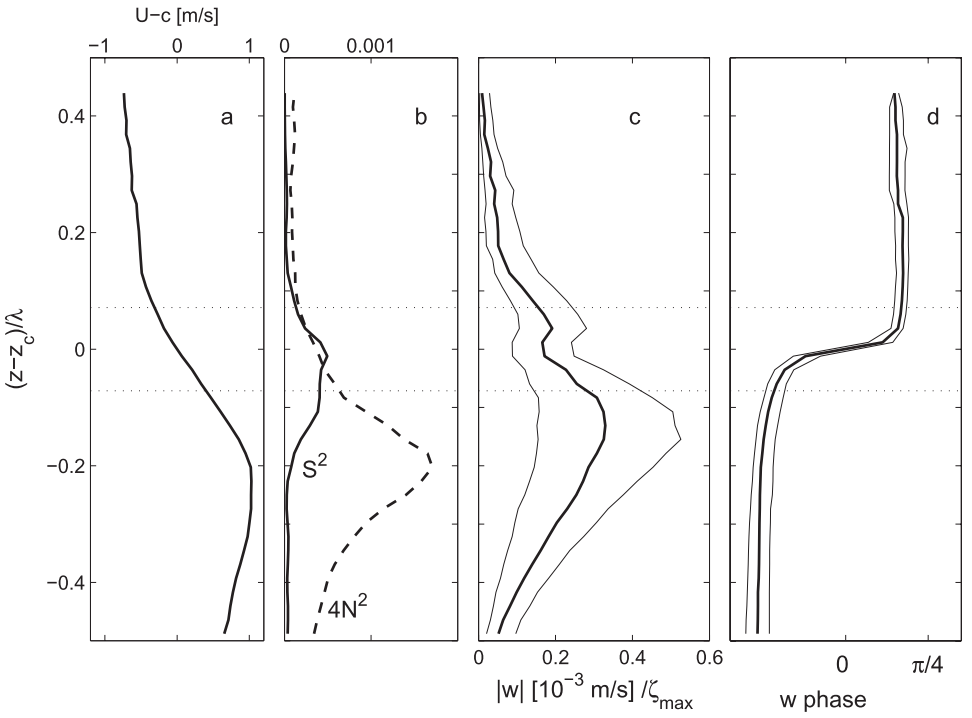

FIG. 7. (a) Median composite velocity $U - c$ from Fig. 6. (b) Median composite S^2 (solid) and $4N^2$(dashed). (c) Composite amplitude of the vertical velocity eigenfunction normalized by the maximum vertical displacement. (d) Composite phase of the vertical velocity eigenfunction. Thick (thin) curves indicate the median (and upper and lower quartiles) of profiles around a sampling of 68 unstable modes. Profiles are centered at the critical level, and the vertical coordinate is normalized by the wavelength. Horizontal dotted lines indicate a layer of thickness $1/7$ the wavelength.

While the perturbation equations of linear theory are homogeneous and therefore cannot predict amplitudes, they often do well at predicting nondimensional ratios, a capacity that has not been much exploited (e.g., Smyth and Kimura 2007). Here, we will use it to allow a comparison of these fluxes with the observations described in Part I. We have scaled the eigenfunctions by the maximum vertical displacement $\zeta_{\max}$, so that the flux quantities plotted are actually ratios of the flux to $\zeta_{\max}^2$. If we have some independent means of determining the maximum vertical displacement, we can make a quantitative estimate of the flux just as the wave attains nonlinear amplitude. To test this idea, we assume that a typical maximum vertical displacement is 10 m. Dillon et al. (1989) quoted a range of momentum fluxes from 10^{-6} to 10^{-5} m^2 s^{-2} in the upper equatorial Pacific (Table 1). When multiplied by 100 to account for a 10-m amplitude, our maximum value becomes 4×10^{-6} m^2 s^{-2}, well within the observed range. Below the critical layer, this flux decays rapidly to about one-half its maximum value, then more slowly, indicating that wavelike motions are carrying eastward momentum down into the EUC.

We next compare the buoyancy flux with observations of the turbulent kinetic energy dissipation rate ϵ from Part I. To see the relationship between these quantities, note that the flux represents an available potential energy gain due to the vertical displacement of isopycnals by growing billows. The resulting energy goes almost entirely into turbulent kinetic energy when the billows break. Of that, a small fraction (the flux Richardson number, typically 0.2) goes into irreversible potential energy gain, while the rest is dissipated. We therefore expect the reversible buoyancy flux due to the growing instability to match the turbulence dissipation rate, at least in an order of magnitude sense. When multiplied by 100, the maximum predicted buoyancy flux is 3×10^{-8} m^2 s^{-3}, well within the observed range of ϵ (Part I).

We have seen that linear eigenmodes contain one-half the information needed to predict numerous useful quantities, including momentum flux and dissipation—the other half being an estimate of the maximum vertical displacement attained before breaking. Here, we have attempted only order-of-magnitude estimates. With better assessments of the breaking amplitude, this method could provide

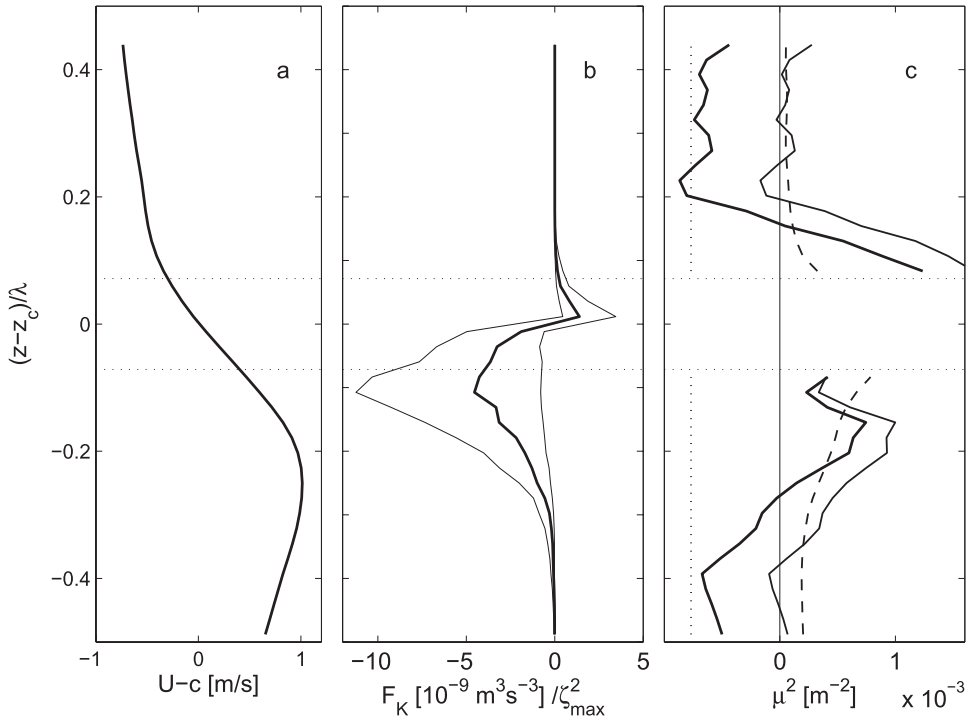

FIG. 8. Energy flux and factors contributing to vertical propagation. (a) Median composite U. (b) Composite vertical kinetic energy flux: median and quartiles. (c) Terms in μ^2, as given in (2), derived from median composite profiles and the median of $\tilde{k}$. Line scheme is thin solid, $N^2/(U-c)^2$; dashed, $-U_{zz}/(U-c)$; dotted, $-\tilde{k}^2$ (constant); and thick solid, μ^2, the sum. Values near the critical level are masked. Horizontal dotted lines indicate a layer of thickness $^1/_7$ the wavelength.

a useful view of the variability of turbulence based on mooring data.

5. The apparent frequency of a quasi-random ensemble of shear instabilities

We have established that the computed instability events are usefully understood in terms of the standard properties of KH instability on a shear layer. The frequency of a KH billow train depends on the wavelength and on the relative velocity between the mean flow and the measuring instrument. Given the wide range of wavelengths and background current velocities, there is no obvious reason why a narrow band of frequencies should be preferred. The peak in frequency could be taken to imply a correlation between wavelength and phase velocity (since $f = c/\lambda$), but such a correlation is not expected a priori.

In fact, a wavelength–phase velocity correlation is not needed to explain the frequency peak, as we now show using a simple probabilistic model. We begin by noting that both the wavelength and phase velocity are inherently band limited. Wavelengths are bounded from above as a multiple (typically 7) of the thickness of the sheared zone between the surface and the EUC. In view of the semicircle theorem (Howard 1961), phase velocities are bounded by the maximum westward SEC and the maximum eastward EUC. We now demonstrate that simple distributions with these characteristics can result in a peaked distribution of frequencies similar to the results of the stability analysis and the observations. We also give a formula for estimating the peak frequency and show that, despite the fact that the oscillations are by construction not gravity waves, the peak frequency is expected to be of order N.

a. The frequency distribution

Consider a collection of instability events with wavelengths distributed uniformly between 0 and λ_0,

$$P_\lambda(\lambda) = \frac{1}{\lambda_0}\begin{cases}1, & \text{if} \quad \lambda < \lambda_0\\ 0, & \text{otherwise}\end{cases}, \tag{3}$$

and phase velocities distributed evenly between u_1 and u_2,

$$P_c(c) = \frac{1}{\Delta u}\begin{cases}1, & \text{if} \quad u_1 < c < u_2\\ 0, & \text{otherwise}\end{cases}, \tag{4}$$

where $\Delta u = u_2 - u_1$.

Assuming that phase velocity and wavelength are independent random variables, P_c and P_λ can be combined

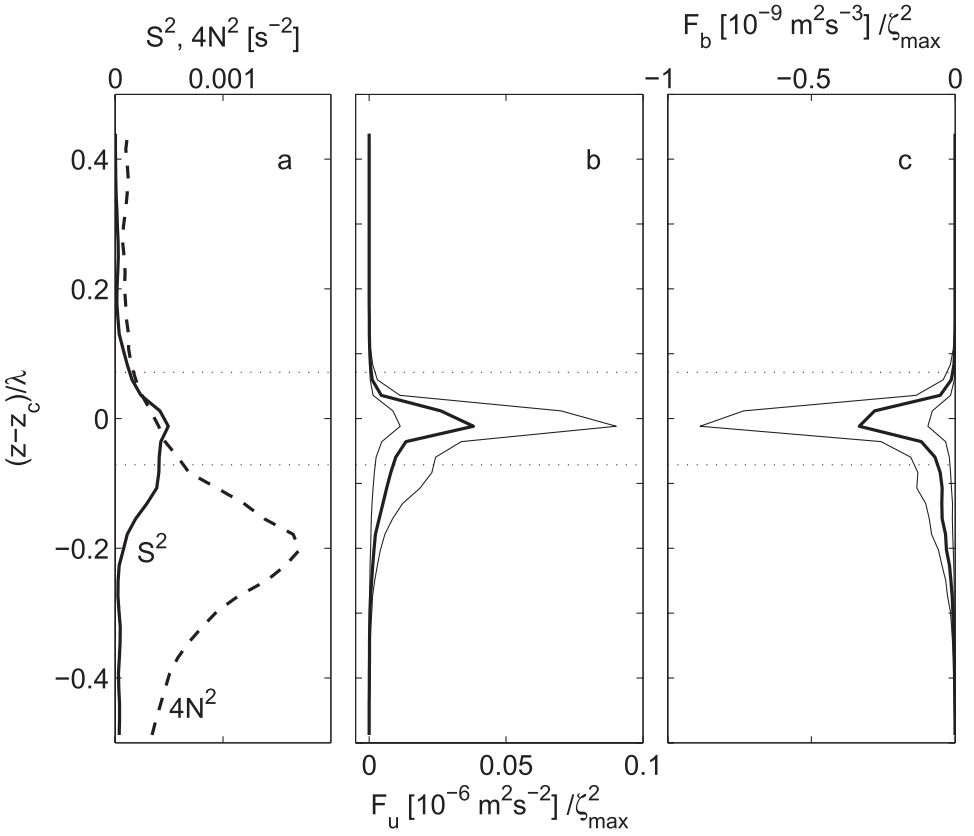

FIG. 9. Momentum and buoyancy fluxes. (a) Median composite S^2 (solid), $4N^2$ (dashed) from Fig. 6 for reference. Composite vertical fluxes of specific (b) momentum and (c) buoyancy. Thick (thin) curves indicate the median (and upper and lower quartiles) of profiles around a sampling of 69 unstable modes. Profiles are centered at the critical level, and the vertical coordinate is normalized by the wavelength. Horizontal dotted lines indicate a layer of thickness $1/7$ the wavelength. Eigenfunctions are normalized so that the maximum vertical displacement is 1 m.

(e.g., Mood et al. 1974) to give the probability density function for the frequency $f = c/\lambda$:

$$P_f(f) = \int_0^\infty \lambda P_\lambda(\lambda) P_c(f\lambda)\, d\lambda$$

$$= \frac{\lambda_0}{2\Delta u}\left\{\begin{array}{lll} 1, & \text{if} & \dfrac{u_1}{\lambda_0} \le f \le \dfrac{u_2}{\lambda_0} \\ \dfrac{u_1^2}{\lambda_0^2 f^2}, & \text{if} & f < \dfrac{u_1}{\lambda_0} \\ \dfrac{u_2^2}{\lambda_0^2 f^2}, & \text{if} & f > \dfrac{u_2}{\lambda_0} \end{array}\right\}. \quad (5)$$

The probability density function for $\log_{10}|f|$, in variance-preserving form, is

$$P_{\log_{10}|f|} = \ln 10 f[P_f(f) + P_f(-f)], \quad (6)$$

which rises to maxima at $|f| = |u_1|/\lambda_0$ and $|f| = |u_2|/\lambda_0$ with the high frequency having the higher probability. The most probable frequency is therefore given by

$$|f| = \frac{\max(|u_1|, u_2)}{\lambda_0}. \quad (7)$$

We show two illustrative cases in Fig. 10. In each case, we let $\lambda_0 = 700$ m (approximately 7 times the depth of the EUC core), and $u_2 = 1$ m s^{-1} (a typical EUC velocity). We make two choices for u_1, the SEC speed. The solid curve shows $u_1 = -1$ m s^{-1}, a relatively large SEC speed found early in this observation period (Fig. 2a). For the second case (dashed curve) we set $u_1 = -0.5$ m s^{-1},

TABLE 1. Comparison of momentum and buoyancy fluxes inferred from linear theory with corresponding observational estimates.

	F_u	F_b
Unit	m^2 s^{-2}	m^2 s^{-3}
$\zeta_{max} = 1$ m	4×10^{-8}	3×10^{-10}
$\zeta_{max} = 10$ m	4×10^{-6}	3×10^{-8}
Obs range	$10^{-6} - 10^{-5}$	$10^{-8} - 10^{-6}$
Source	Dillon et al. (1989)	Part I

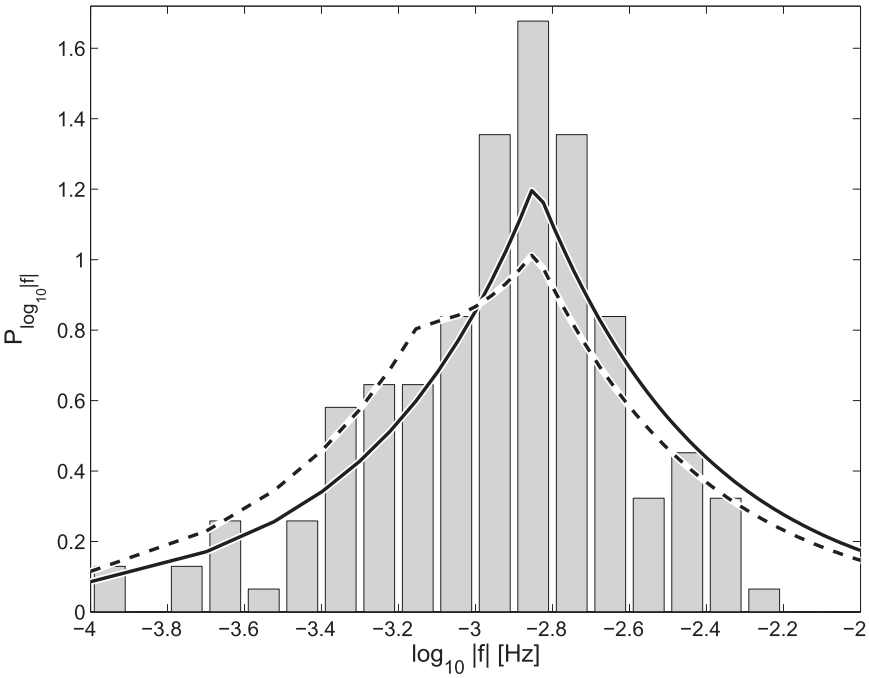

FIG. 10. Model probability density function described in (5) and (6). Parameter values are $\lambda_0 = 700$ m, $u_2 = 1$ m s^{-1}, $u_1 = -1$ m s^{-1} (solid curve), and $u_1 = -0.5$ m s^{-1} (dashed curve). Shown in the background is the distribution of the computed mode frequencies.

a more typical SEC speed. In both cases, the predicted peak frequency u_2/λ_0 agrees with the direct computations to within about a factor $10^{0.1}$, or 25%. In the second case, a second peak correlates well with the negative skewness of the eigenmode frequencies. Recall that this negative skewness is also evident in the observations (Fig. 1).

The close agreement seen in Fig. 10 must be somewhat fortuitous due to the strong assumptions that underlie both the numerical stability analyses and the theory. In particular, the maximum wavelength of 700 m results from thinking of the layer between the EUC core and the surface as a free shear layer whose most unstable mode should have wavelength 7 times its thickness. The reality is more complex than this, especially due to the proximity of the surface. In addition, the uniform distributions of wavelength (3) and frequency (4) represent significant oversimplifications.[2] The numerical stability results have their own limitations (as described in section 3) and may miss a large fraction of the instability events. The close comparison with the peak frequency of the measured spectra in Fig. 1, however, encourages us to conclude that the simple theory expressed in (5) and (6) has some truth to it, and the estimates from (7) of the peak frequency are useful to within, say, a factor of 2.

b. *Why is* $\boldsymbol{\omega} \sim$ N *preferred?*

Although the frequency of a KH instability is virtually independent of stratification, the correspondence between the observed narrowband frequencies and the local buoyancy frequency is striking (see Part I). We now show that this correspondence is an expected property of a random ensemble of KH instability events under certain conditions. The peak frequency derived in the previous subsection is given in radians per second as

$$\omega_{\text{peak}} = 2\pi f_{\text{peak}} = \frac{\max(|u_1|, u_2)}{\lambda_0/2\pi}. \tag{8}$$

Our objective is to show that $\omega_{\text{peak}} \sim O(N)$.

We begin by arguing that $\omega_{\text{peak}} \sim O(S)$. The maximum possible thickness of the random layers of enhanced shear is approximately D, the depth of the EUC core. Assuming that the resulting instabilities have the spatial scale of KH billows, the maximum possible wavelength is then $\lambda_0 \approx 7D$. As a result, we can approximate (8) as

[2] In appendix B, a refined theory is developed based on more realistic distributions of λ and c. The refined theory offers no better agreement with numerical or observational results. The peak frequency is essentially unchanged from (7), though its value must be computed numerically. Thus, we retain the simpler theory expressed in (5) and (6) for the remainder of the paper.

$$\omega_{\text{peak}} \approx \frac{\max(|u_1|, u_2)}{D}. \tag{9}$$

We assume next that the reference frame in which the oscillations are measured moves at a velocity between u_1 and u_2, and define that velocity as zero so that $u_1 < 0$ while $u_2 > 0$. The absolute mean shear can be written as

$$S \approx \frac{\Delta u}{D} = \frac{u_2 + |u_1|}{D}. \tag{10}$$

How does this compare with the ratio in (9)? The numerator of (10) is the sum of two positive numbers, and the larger of those two is the numerator of (9). Because the larger of two positive numbers must be at least half of their sum, ω_{peak} lies between the approximate bounds $S/2$ and S. It suffices to conclude that

$$\omega_{\text{peak}} \sim O(S). \tag{11}$$

The connection to stratification is now made via the Richardson number. Because instability events typically occur when Ri is depressed to values less than about 1/4, we expect a priori that the mean flow will have Ri not much greater than this. In fact, observations in the upper equatorial oceans routinely show mean flows with Ri $\sim O(1)$ (e.g., Fig. 7c in Part I). On this basis, we expect $S \sim O(N)$, and (11) therefore becomes

$$\omega_{\text{peak}} \sim O(N). \tag{12}$$

We emphasize that the correspondence between the peak frequency and N has nothing to do with the physics of internal gravity waves. It is instead a result of the following assumptions.

- A random ensemble of KH-like instability events exhibits an even distribution of wavelength and phase velocity.
- The mean flow is characterized by Ri $\sim O(1)$.
- Oscillations are measured from a reference frame moving at a velocity that is within range of the mean flow.

6. Conclusions

In Part I, we analyzed extended, high-resolution time series of temperature at four depths: 29, 39, 49, and 59 m. Each series showed a persistent spectral peak near the angular cyclic frequency 1.4 mHz. These oscillations showed several ''textbook'' features of KH instability; that is, the phase shift, wavelength, and phase velocity were all consistent with Hazel's (1972) analysis of a hyperbolic tangent shear layer. One feature remained unexplained, though, namely the existence of a preferred frequency of order N. KH instabilities have no preferred frequency, and the frequency of any given KH mode is essentially independent of stratification.

To interpret these observed oscillations, we have imagined that the sheared zone between the surface and the EUC core is generally close to a neutral equilibrium Ri $\sim O(1)$ (Figs. 11a and 11b). We further suppose that this equilibrium is upset sporadically so as to cause an instability. To test this notion, we have used an ensemble of 155 instability events computed from hourly averaged profiles. As expected, critical levels are clustered on the strongly sheared upper flank of the EUC (Fig. 11c). The frequency distribution (Fig. 1) compares extremely well with spectra from the four independent sensors, and we interpret this as evidence that the observed oscillations are indeed driven by instabilities.

We have constructed composite mean flow and eigenfunction profiles that are broadly consistent with the KH model. We have also seen, however, that the mean flow and eigenfunctions differ from the ''tanh'' model in some significant ways. In particular, the shear layer is underlain by a stratified jet (Figs. 11a and 11b), which supports downward radiation. The ''near jet'' model used in the nonlinear simulations of Pham and Sarkar (2010) may provide an improved representation of this mean flow. We have seen that eigenfunctions of the momentum and buoyancy fluxes, combined with an estimate of billow amplitude, give quantitative estimates of those fluxes that compare reasonably well with the observations. With a more detailed assessment of the amplitudes, this could provide a useful way to estimate these fluxes based on mooring data only.

We have explained the near-N frequency peak in terms of a probabilistic model of an ensemble of KH instability events having a range of wavelengths $\lambda \in (0, \lambda_0]$ bounded by Hazel's (1972) results and phase speeds $c \in (u_1, u_2)$ bounded by the semicircle theorem (Howard 1961). Assuming that the wavelength and phase velocity are distributed uniformly within these limits, we have shown that the absolute frequency is distributed in accordance with (5) and (6). In a variance-preserving representation, there is a peak at frequency $\max(|u_1|, u_2)/\lambda_0$, and a secondary peak at $\min(|u_1|, u_2)/\lambda_0$. If $|u_1| = u_2$, or if either velocity is zero, there is only one peak. The peak frequency compares well with both explicit linear stability analyses and with the χpod observations. The secondary peak is always at a lower frequency and may, therefore, explain the negative skewness in both the unstable modes and observed oscillations.

An order-of-magnitude estimate reveals that the peak angular frequency ω_{peak} is likely to be of the same order as the mean shear. Recognizing that strongly sheared geophysical flows are often characterized by Ri $\sim O(1)$ (as is shown explicitly for this case in Part I), we conclude that the peak angular frequency is indeed expected to be of order N. The strongest assumptions underlying this prediction are that

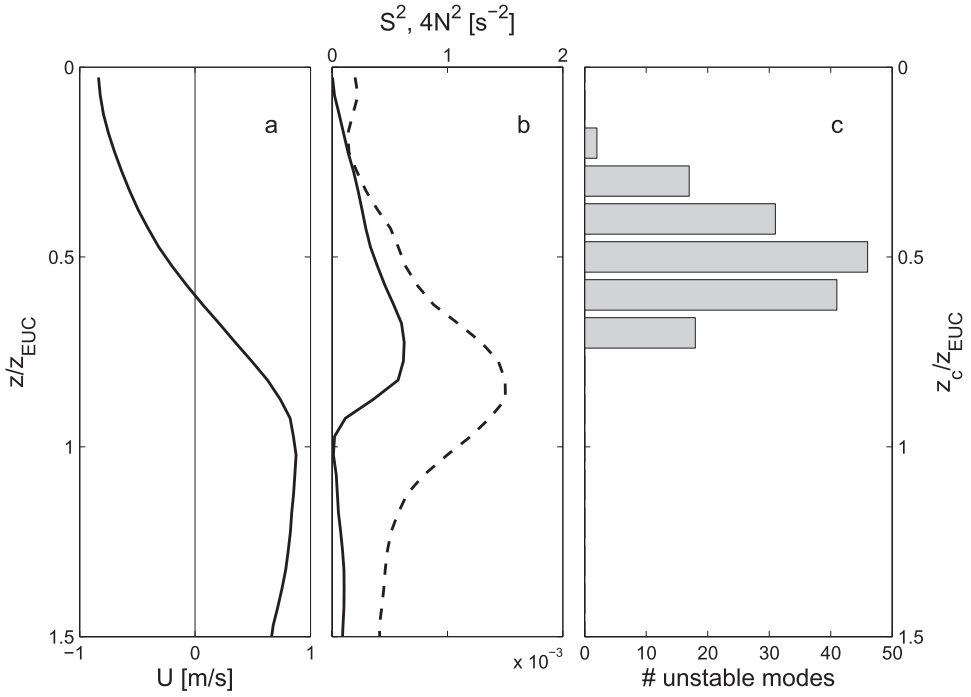

FIG. 11. (a) Median U against a vertical coordinate scaled by the undercurrent depth. (b) Median S^2 (solid) and $4N^2$ (dashed). (c) Histogram of critical levels for 155 unstable modes.

- a strongly sheared, stratified flow is destabilized by random events and
- the observer is moving at a speed within the range of the mean current profile.

We therefore suggest that near-N oscillations in strongly sheared regimes may be an indication of random shear instability in a marginally unstable environment.

Acknowledgments. This work has benefited from helpful conversations with M. Hoecker-Martinez and critical readings by S. Thorpe, Zhiyu Liu, and two anonymous reviewers. The project was funded by the National Science Foundation via Grants 0424133, 0622922, and 0728375.

APPENDIX A

Computing Normal Modes of a Viscous, Diffusive, Stratified Shear Flow

Here, we describe in detail the theory and numerical methods used for the stability analyses. Space is measured by the Cartesian coordinates x, y, and z and the corresponding unit vectors **i**, **j** and **k** denoting the eastward, northward, and vertical directions, respectively. Planetary rotation is neglected. The fluid is incompressible, viscous, diffusive, and stratified such that the Boussinesq approximation applies. The buoyancy is defined by $b = -g(\rho - \rho_0)/\rho_0$, where ρ is the density with characteristic value ρ_0 and g is the acceleration due to gravity. The resulting equations of motion are

$$\nabla \cdot \mathbf{u} = 0,$$

$$\frac{D\mathbf{u}}{Dt} = -\nabla p + b\mathbf{k} + \nu\nabla^2\mathbf{u}, \quad \text{and}$$

$$\frac{Db}{Dt} = \kappa\nabla^2 b,$$

in which **u** is the velocity vector,

$$\frac{D}{Dt} = \frac{\partial}{\partial t} + \mathbf{u}\cdot\nabla$$

is the material derivative, t is the time, and p is the pressure scaled by ρ_0. The viscosity ν and the mass diffusivity κ may be either molecular or turbulent in origin, but are assumed to be constants.

Substituting the perturbation solution

$$\mathbf{u} = U(z,t)\mathbf{i} + V(z,t)\mathbf{j} + \varepsilon\mathbf{u}' \quad \text{and}$$

$$b = B(z,t) + \varepsilon b'; \quad p = P(z,t) + \varepsilon p',$$

we obtain, at order unity,

$$\frac{\partial U}{\partial t} = -\frac{\partial P}{\partial x} + \nu\frac{\partial^2 U}{\partial z^2}, \frac{\partial V}{\partial t} = -\frac{\partial P}{\partial y} + \nu\frac{\partial^2 V}{\partial z^2},$$

$$0 = \frac{\partial P}{\partial z} + B, \quad \text{and} \quad \frac{\partial B}{\partial t} = \kappa\frac{\partial^2 B}{\partial z^2}.$$

For the background flow to be in steady state, we must make the following assumptions.

- The zonal pressure gradient balances the action of viscosity on the mean flow U, V, possibly because both are negligible.
- The vertical pressure gradient is in hydrostatic balance with the background buoyancy profile.
- The action of diffusion on the mean buoyancy profile B is negligible. More specifically, the mean profile cannot vary significantly on the time scale of instability growth.

The $O(\epsilon)$ equations are combined into a pair of equations for w' and b', into which we substitute the normal mode forms described in (1) and the accompanying discussion. To simplify the computations, we define the rotated background velocity

$$\tilde{U} = (kU + lV)/\tilde{k}, \tag{A1}$$

where the wave-vector magnitude $\tilde{k}$ is as defined in section 3.

The $O(\epsilon)$ equations can then be written as

$$\sigma\begin{pmatrix}\nabla^2 & 0\\ 0 & I\end{pmatrix}\begin{pmatrix}\hat{\omega}\\ \hat{b}\end{pmatrix} = \begin{pmatrix}-i\tilde{k}\tilde{U}\nabla^2 + i\tilde{k}\tilde{U}_{zz} + \nu\nabla^4 & -\tilde{k}^2\\ -B_z & -i\tilde{k}\tilde{U} + \kappa\nabla^2\end{pmatrix}\begin{pmatrix}\hat{w}\\ \hat{b}\end{pmatrix}, \tag{A2}$$

where the subscript z indicates a vertical derivative and the Laplacian is given by

$$\nabla^2 = \frac{d^2}{dz^2} - \tilde{k}^2. \tag{A3}$$

Boundary conditions are $\hat{\omega} = \hat{b} = 0$.

While stability analyses are often accomplished using shooting methods (e.g., Hazel 1972; Sun et al. 1998; Newsom and Banta 2003), those methods become extremely complex with the introduction of viscosity and diffusion. Matrix methods avoid that complexity and also guarantee (within the limits of resolution) that all relevant modes will be found. The eigenfunctions $\hat{w}$ and $\hat{b}$ are discretized on N points (z_i; $i = 1, 2, \ldots, N$) and the derivative with respect to z is approximated by a second-order finite difference.[A1] The Laplacian (A3) is now expressible as a matrix, and (A2) forms a generalized eigenvalue problem that can be solved using standard methods.

Eigenfunctions for the horizontal velocity and the scaled pressure are defined as in (1) and recovered using the following polarization relations:

$$\hat{\tilde{u}} = \frac{i}{\tilde{k}}\hat{w}_z \quad \text{and} \tag{A4}$$

$$\hat{p} = \frac{i}{\tilde{k}}\left[\tilde{U}_z\hat{w} + (c - \tilde{U})\hat{w}_z - \frac{i}{\tilde{k}}\nu\nabla^2\hat{w}_z\right]. \tag{A5}$$

Here, $\hat{\tilde{u}} = (k\hat{u} + l\hat{v})/\tilde{k}$ is the rotated perturbation velocity analogous to (A1). The rotation is reversed to give the individual perturbation velocity eigenfunctions:

$$\hat{u} = \hat{\tilde{u}}\cos\theta; \quad \upsilon = \hat{\tilde{u}}\sin\theta,$$

where the angle of obliquity is $\theta = \tan^{-1}(l/k)$.

Vertical fluxes of horizontal velocity, kinetic energy, and buoyancy are given by

$$F_u = \overline{u'w'}; \quad F_v = \overline{v'w'}, \tag{A6}$$

$$F_K = \overline{p'w'}, \quad \text{and}$$

$$F_b = \overline{b'w'}.$$

The overbar indicates a horizontal average over one wavelength.

APPENDIX B

Refined Statistical Theory of a KH Ensemble

In this appendix we refine two assumptions underlying of the ensemble theory discussed in section 5a, namely that wavelength and phase velocity are uniformly distributed. In fact, shorter wavelengths are expected to be more numerous simply because they grow on thinner shear layers, and hence the sheared zone between the surface and the EUC core can accommodate more of

[A1] The discretization has been the object of considerable experimentation. Higher-order methods, both finite difference and compact, deliver no increase in the accuracy of the eigenmodes. A similar result was found for a related problem by Putrevu and Svendsen (1992).

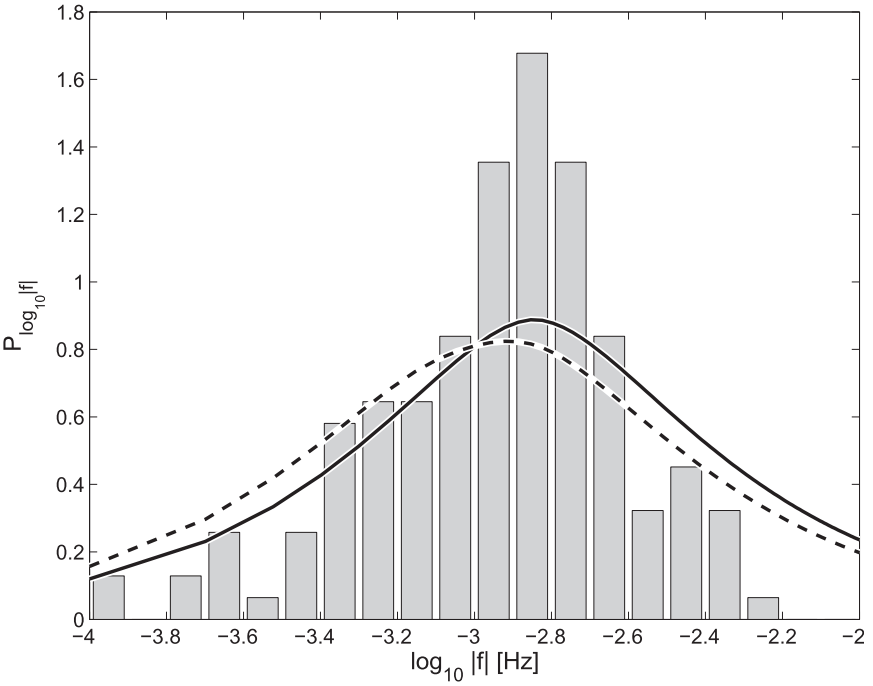

FIG. B1. Model probability density function described in (6), in variance-preserving form. Parameter values are $\lambda_0 = 400$ m, $u_2 = 1$ m s^{-1}, $u_1 = -1$ m s^{-1} (solid curve), and $u_1 = -0.5$ m s^{-1} (dashed curve). Shown in the background is the distribution of computed mode frequencies.

them. To express this assumption simply, we allow the distribution to decrease linearly to zero at $\lambda = \lambda_0$:

$$P_\lambda(\lambda) = \frac{2}{\lambda_0}\left\{\begin{array}{ll} 1 - \dfrac{\lambda}{\lambda_0}, & \text{if} \quad 0 \le \lambda \le \lambda_0 \\ 0 & \text{otherwise.} \end{array}\right\}$$

As for the phase velocity distribution, unstable modes are expected to be most numerous where the background shear is strongest, that is, near the center of the sheared zone where mean flow velocities are small. Since modes in that zone will have small phase velocities, we expect that the distribution of c will be larger at small c and smaller near the limiting values u_1 and u_2. In view of this, we replace (4) with the triangular distribution

$$P_c(c) = \frac{2}{\Delta u}\begin{cases} 1 + \dfrac{c}{u_1}, & \text{if} \quad u_1 < c < 0 \\ 1 - \dfrac{c}{u_2}, & \text{if} \quad 0 < c < u_2 \\ 0, & \text{otherwise} \end{cases}.$$

Both of these refinements are supported by the histograms of the computed unstable modes shown in Figs. 5d and 5f. We caution against assigning too much significance to this, though, because the numerical analysis does not capture all possible modes.

Combining these distributions as before, we obtain

$$P_f(f) = \frac{\lambda_0}{3\Delta u}\begin{cases} \left(2 + \dfrac{|u_1|}{\lambda_0 f}\right)\left(\dfrac{u_1}{\lambda_0 f}\right)^2, & \text{if} \quad f \le -\dfrac{|u_1|}{\lambda_0} \\ 2 + \dfrac{\lambda_0 f}{|u_1|}, & \text{if} \quad -\dfrac{|u_1|}{\lambda_0} < f < 0 \\ 2 + \dfrac{\lambda_0 f}{u_2}, & \text{if} \quad 0 \le f \le \dfrac{u_2}{\lambda_0} \\ \left(2 - \dfrac{u_2}{\lambda_0 f}\right)\left(\dfrac{u_2}{\lambda_0 f}\right)^2, & \text{if} \quad f \ge \dfrac{u_2}{\lambda_0} \end{cases},$$

which is manipulated to form the variance-preserving spectrum of $|f|$ as before.

Figure B1 shows two examples, superimposed on the histogram of the computed instabilities as in Fig. 10. Based on Fig. 5f, we choose $\lambda_0 = 400$ m. Surprisingly, the refined theory is less consistent with the numerical results than the simpler model. The peak frequency must be computed numerically, but it is always between 0.85 and 1.0 times $\max(|u_1|, u_2)/\lambda_0$. Thus, the essential prediction from the simpler theory is unchanged. We conclude that the added complexity of the refined theory is not justified, and that the simpler approach leading to (5)–(7) is preferable.

REFERENCES

Dillon, T., J. Moum, T. Chereskin, and D. Caldwell, 1989: Zonal momentum balance at the equator. *J. Phys. Oceanogr.,* **19,** 561–570.

Hazel, P., 1972: Numerical studies of the stability of inviscid parallel shear flows. *J. Fluid Mech.,* **51,** 39–62.

Hebert, D., J. Moum, C. Paulson, and D. Caldwell, 1992: Turbulence and internal waves at the equator. Part II: Details of a single event. *J. Phys. Oceanogr.,* **22,** 1346–1356.

Howard, L., 1961: Note on a paper of John W. Miles. *J. Fluid Mech.,* **10,** 509–512.

Miles, J., 1961: On the stability of heterogeneous shear flows. *J. Fluid Mech.,* **10,** 496–508.

Mood, A. M., F. A. Graybill, and D. C. Boes, 1974: *Introduction to the Theory of Statistics*. 3rd ed. McGraw-Hill, 480 pp.

Moum, J., D. Hebert, C. Paulson, and D. Caldwell, 1992: Turbulence and internal waves at the equator. Part I: Statistics from towed thermistor chains and a microstructure profiler. *J. Phys. Oceanogr.,* **22,** 1330–1345.

——, J. Nash, and W. Smyth, 2011: Narrowband oscillations in the upper equatorial ocean. Part I: Interpretation as shear instabilities. *J. Phys. Oceanogr.,* **41,** 397–411.

Newsom, R., and R. Banta, 2003: Shear flow instability in the stable nocturnal boundary layer as observed by Doppler lidar during CASES-99. *J. Atmos. Sci.,* **60,** 16–33.

Peters, H., M. Gregg, and T. Sanford, 1994: The diurnal cycle of the upper equatorial ocean: Turbulence, fine-scale shear, and mean shear. *J. Geophys. Res.,* **99,** 7707–7723.

Pham, H. T., and S. Sarkar, 2010: Internal waves and turbulence in a stable stratified jet. *J. Fluid Mech.,* **648,** 297–324.

Putrevu, U., and A. Svendsen, 1992: Shear instability of longshore currents: A numerical study. *J. Geophys. Res.,* **97,** 7283–7303.

Skyllingstad, E., and D. Denbo, 1994: The role of internal gravity waves in the equatorial current system. *J. Phys. Oceanogr.,* **24,** 2093–2110.

Smyth, W., and J. Moum, 2002: Shear instability and gravity wave saturation in an asymmetrically stratified jet. *Dyn. Atmos. Oceans,* **35,** 265–294.

——, and S. Kimura, 2007: Instability and diapycnal momentum transport in a double-diffusive stratified shear layer. *J. Phys. Oceanogr.,* **37,** 1551–1565.

Sun, C., W. Smyth, and J. Moum, 1998: Dynamic instability of stratified shear flow in the upper equatorial Pacific. *J. Geophys. Res.,* **103,** 10 323–10 337.

Wang, D., and P. Müller, 2002: Effects of equatorial undercurrent shear on upper-ocean mixing and internal waves. *J. Phys. Oceanogr.,* **32,** 1041–1057.

——, J. McWilliams, and W. Large, 1998: Large eddy simulation of the diurnal cycle of deep equatorial turbulence. *J. Phys. Oceanogr.,* **28,** 129–148.